CHEMISTRY OF MATERIALS

ARTICLE

pubs.acs.org/cm

# Preparation and Characterization of PdFe Nanoleaves as Electrocatalysts for Oxygen Reduction Reaction

Zhiyong Zhang,[†] Karren L. More,[‡] Kai Sun,[§] Zili Wu,[⊥] and Wenzhen Li*[,†]

[†]Department of Chemical Engineering, Michigan Technological University, Houghton, Michigan 49931, United States

[‡]Materials Science and Technology Division, Oak Ridge National Laboratory, Oak Ridge, Tennessee 37831, United States

[§]Department of Materials Science and Engineering, University of Michigan, Ann Arbor, Michigan 48109, United States

[⊥]Center for Nanophase Materials Sciences, Oak Ridge National Laboratory, Oak Ridge, Tennessee 37831, United States

Supporting Information

**ABSTRACT:** Novel PdFe-nanoleaves (NLs) have been prepared through a wet chemistry-based solution phase reduction synthesis route. High-resolution transmission electron microscopy (HR-TEM) and scanning transmission electron microscopy (S/TEM) coupled with high-spatial-resolution compositional analysis clearly show that this newly developed structure is assembled from Pd-rich nanowires (Pd-NWs) surrounded by Fe-rich sheets. The Pd-NWs have diameters in the range of 1.8−2.3 nm and large electrochemical surface areas of >50 $m^2/g$. Their length (30−100 nm) and morphology can be tuned by altering the nanostructure synthesis conditions and the Fe amount in the NLs. With increasing Fe content, thinner and longer sheet-enveloped nanowires can be prepared. The side surfaces of Pd-NWs observed by HR-TEM are predominantly Pd(111) facets, while the tips and ends are Pd(110) and Pd(100) facets. By etching away the enveloping Fe-rich sheets using an organic acid, the Pd-rich NWs are exposed on the surfaces of the nanoleaves, and they demonstrate high reactivity toward electrocatalytic reduction of oxygen in a 0.1 M NaOH electrolyte, i.e., a factor of 3.0 increase in the specific activity and a factor of 2.7 increase in the mass activity, compared to a commercial Pt/C catalyst (at 0 V vs. Hg/HgO). The electrocatalytic activity enhancement can be attributed to the unique nanoleave structure, which provides more Pd(111) facets, a large surface area, and more resistance to Pd oxide formation.

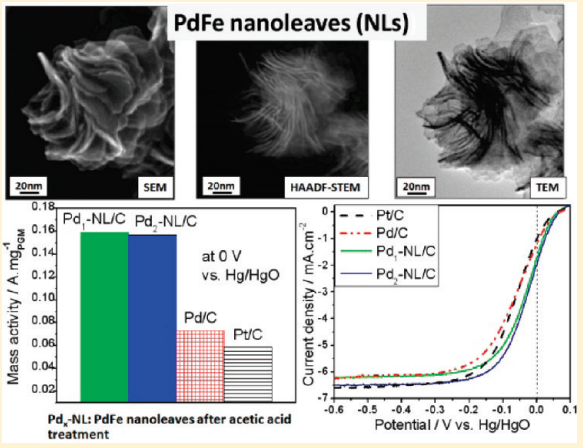


**KEYWORDS:** electrocatalyst, nanoleaves, Pd−Fe, oxygen reduction, solution phase synthesis, alkaline electrolyte

## INTRODUCTION

Without the Carnot cycle limitation, low-temperature proton exchange membrane fuel cells (PEMFCs) directly convert the chemical energy of fuels into electricity with high theoretical efficiency (i.e., 83% for $H_2$ fuel at a thermodynamic potential of 1.229 V under standard conditions) and zero emission; therefore, they are considered to be a promising sustainable power source.[1] However, the sluggish kinetics of the oxygen reduction reaction (ORR) at the cathode remains a great scientific challenge that hinders the high energy conversion efficiency of PEMFCs.[2] Platinum group metal (PGM)-based electrocatalysts are currently used for PEMFCs to reduce the large ORR overpotential.[2c−e] Unfortunately, even on the most active Pt surface, the overpotential is >250 mV at open circuit voltage (OCV). The thermodynamic efficiency drops from 83% (1.229 V) to, i.e., 66% at an OCV value of 0.98 V under standard conditions.[1a,2] Since the exchange current density of the ORR is very small ($10^{-9}$ $A/cm^2$ at the Pt surface),[2e] to get a usable output current, the operating voltage must be largely reduced to, i.e., 0.65 V, making the energy efficiency of PEMFCs decrease further to 44%.

PGM-based multimetallic nanostructures with well-controlled size, shape, structure, chemical composition, and morphology can effectively enhance the catalytic reaction kinetics through modifying surface compositions, optimizing highly active crystalline facets, and tuning electronic structures.[3] Wet-chemical synthesis (WCS) approaches have emerged as one of the most promising methods to control the surface facets and electronic properties of the PGM nanostructures accurately.[4] Various Pt-based nanostructures, such as nanowires,[5] nanorods,[3g] nanotubes,[6] monolayer/skin-layer nanoparticles,[7] nanodendrites,[8] hollow nanoparticles,[9] etc., have been synthesized through wet-chemical routes and have demonstrated the ability to improve the ORR activity for PEMFCs. However, the price of

**Received:** November 29, 2010
**Revised:** January 25, 2011
**Published:** February 22, 2011

Pt is very expensive, because of its extremely low reserves in the Earth's crust (0.003 ppb),[10] and it is of critical importance to develop non-Pt catalysts to enable the widespread application of PEMFCs for use in automotive and stationary applications. The abundance of Pd is 200 times greater than Pt and the price of Pd is only 20%−25% of that of Pt, which makes Pd a realistic alternative as a fuel cell catalyst. In low pH media, Pd-based alloy catalysts have demonstrated comparable ORR activity;[11] however, the ORR exchange current density for Pd is only $10^{-10}$ A/cm$^2$, and its intrinsic ORR activity (i.e., at 0.9 V vs RHE (reversible hydrogen electrode)) is nearly an order of magnitude lower than that of Pt.[12] Furthermore, the durability of Pd-based catalysts remains a big concern for acid electrolyte fuel cell applications.[2b]

It has been found that the ORR kinetics can be significantly enhanced as a result of improved charge/ion transfer in alkaline electrolytes.[13] Recently, novel solid alkaline membranes have been developed and demonstrated a high anion exchange conductivity,[14] thereby making low-temperature anion exchange membrane fuel cells more attractive for ORR catalysts in high pH media. Pd is reported to possess a competitive intrinsic ORR activity with Pt, which is attributed to lower peroxide yields at the mixed kinetic-diffusion control region.[13h] Pt(111) single crystals covered by a monolayer of Pd has demonstrated higher intrinsic ORR activity than Pt(111) in 0.1 M KOH, which is due to an optimization of the balance between the kinetics of O−O bond breakage and electro-reduction of the intermediates.[13d,e] Pd−Ni alloy nanoparticles are reported to be able to facilitate a high number of electron transfers during oxygen reduction in high pH media, and thus exhibit a comparable ORR activity as Pt, which is attributed to Pd lattice shrinkage due to the incorporation of Ni.[13f] Thus, there is a critical need to explore novel Pd nanostructures with advantageous facets and/or optimized electronic properties to further improve the ORR activity in alkaline electrolyte.

In this article, we report recent research for a simple wet-chemical method to synthesize novel PdFe nanoleaves (PdFe-NLs) with Pd-rich nanowire (Pd-NW) "veins" and Fe-rich "blades" or sheets. The PdFe-NLs with thin Pd-NWs exposed on the surfaces can be achieved by dissolving a majority of the Fe from the NL structure. The formation of the Fe-rich sheets during synthesis can facilitate the formation of uniformly long and thin Pd-NWs. A combination of characterization techniques show that the side surfaces of the Pd-NWs enveloped within the Fe-rich sheets of the NLs are predominantly Pd(111) facets, with Pd(110) and Pd(100) facets only at the tips and ends of the NWs. After the Fe-rich sheets are removed by acetic acid, the fine-scale Pd-NWs are exposed on the surface of nanoleaves with the advantageous crystallographic Pd(111) facets, which demonstrated a 2.7× higher ORR mass activity than commercial Pt/C catalyst in 0.1 M NaOH.

## EXPERIMENTAL SECTION

**Synthesis of $Pd_xFe_y$-NLs.** $Pd_xFe_y$-NLs (Pd:Fe atomic ratio = 1:1, 2:1, and 5:1) were prepared through a solution phase reduction approach.[3g,4j] The synthesis of $Pd_1Fe_1$−NL is described as follows: a mixture of 153 mg of $Pd(acac)_2$ (0.5 mmol) and 20 mL of oleylamine (OAm) was rapidly heated to 105 °C under a blanket of nitrogen, at which time 120 $\mu$L of $Fe(CO)_5$ (1.0 mmol) was immediately injected into the synthesis system. The temperature was held at 105 °C for 20 min, and then increased to 160 °C and held for an additional 30 min. The solution was cooled to room temperature by removing the mantle heater. A mixture of 10 mL of hexane and 50 mL of ethanol was added, and the product was separated by centrifuging at 8000 rpm for 10 min. The product was then cleaned by redispersing it in a mixture of 5 mL of hexane and 25 mL of ethanol and separating by centrifuging three additional times. The final $Pd_1Fe_1$-NL (Pd:Fe atomic ratio = 1:1) sample was stored in 10 mL hexane. Following a similar procedure, 60 $\mu$L (0.5 mmol) and 24 $\mu$L (0.2 mmol) of $Fe(CO)_5$ were injected in the synthesis solutions to prepare $Pd_2Fe_1$-NL and $Pd_5Fe_1$-NL, respectively. To investigate the effect of synthesis conditions on the nanoleaves morphology, 120 $\mu$L of $Fe(CO)_5$ was injected into the system at different temperatures, 60 °C (immediately at this temperature) and 105 °C (after aging at this temperature for 20 min), and the samples were designated $Pd_1Fe_1$-NL-B, and $Pd_1Fe_1$-NL-C, respectively.

**Preparation of Carbon-Supported $Pd_x$-NLs.** An appropriate amount of $Pd_xFe_y$-NL was mixed with 212 mg of carbon black (Vulcan XC-72R) to prepare a carbon-supported $Pd_xFe_y$-NL sample (including $Pd_5Fe_1$-NL/C, $Pd_2Fe_1$-NL/C, and $Pd_1Fe_1$-NL/C) with a Pd loading of ∼20 wt %. To remove the Fe-rich sheets that enveloped the Pd-rich NWs, an organic acid treatment was performed, whereby 100 mg of the as-prepared $Pd_xFe_y$-NL/C sample was dispersed in 20 mL hexane under strong ultrasonication to form a uniform ink, followed by injection of 20 mL acetic acid and heating at 70 °C for 10 h. After the system was cooled to room temperature, 50 mL of acetone was added and the product was separated by centrifuging the mixture at 5000 rpm for 5 min. The product was washed in 20 mL of acetone four times to remove all the acetic acid and then dried at 40 °C overnight. After the organic acid treatment, the resulting product from the $Pd_xFe_y$-NL/C was designated as $Pd_x$-NL/C (since most of Fe has been removed). A control sample, Pd/C (20 wt %), was synthesized via a well-established ethylene glycol reduction (EG) method.[15]

**Characterization.** The composition, morphology, and structure of the NLs were analyzed by X-ray diffraction (XRD), high-resolution transmission electron microscopy (HR-TEM), high-angle annular dark field (HAADF) scanning transmission electron microscopy (S/TEM) coupled with high-spatial-resolution energy dispersive spectroscopy (EDS), scanning electron microscopy (SEM), X-ray photoelectron spectroscopy (XPS), inductively coupled plasma atomic emission spectroscopy (ICP-AES), and thermogravimetric analysis (TGA). XRD patterns were collected by a Scintag XDS-2000 $\theta/\theta$ diffractometer with Cu K$\alpha$ radiation ($\lambda$ = 1.5406 Å), with a tube current of 35 mA and tube voltage of 45 kV. HR-TEM was performed on a JEOL 2040 with an operating voltage of 300 kV. Simultaneous HAADF-STEM, TEM, and SEM imaging was performed using a Hitachi HF3300 TEM/STEM operated at 300 kV. HAADF-S/TEM was also conducted using a probe-corrected (CEOS aberration-corrector) JEOL 2200FS with an operating voltage of 200 kV. High-spatial-resolution EDS compositional analysis (Bruker X-flash silicon drift detector (SDD)) was performed on this microscope using a beam diameter of ∼2 Å and a beam current of ∼1400 pA. XPS spectra were collected using a Thermo Scientific K-Alpha instrument. The NLs were dissolved in aqua regia (a strong acid mixture with HCl:$HNO_3$ volume ratio of 3:1) and the solvent was analyzed by ICP-AES to determine the Pd−Fe bulk compositions. The detection limits for Pd and Fe were 1.0 and 0.1 ppm, respectively. TGA was carried out on SDT Q600 (TA Instruments). The temperature was first increased from room temperature (RT) to 500 °C in $N_2$ at a ramping rate of 10 °C/min. After holding at 500 °C for 10 min, the carrier gas was switched to air and the temperature was further increased to 900 °C at the same ramping rate.

A conventional three-compartment-cell (AFCELL3, Pine Instrument) with a glassy carbon working electrode (GCE), a Hg/HgO reference electrode, and a Pt wire counter electrode, was used for cyclic voltammerty (CV) testing and rotating disk electrode (RDE)-based ORR activity testing of the $Pd_x$-NLs, Pd/C, and a commercial Pt/C (20 wt %, E-TEK)


dx.doi.org/10.1021/cm1034134 |Chem. Mater. 2011, 23, 1570–1577

**Table 1. Summary of Atomic Composition, Length, Diameter, and Lattice Parameter of Pd/C and $Pd_xFe_y$-NLs**

| | atomic composition (by ICP-AES) | surface atomic composition (by XPS) | atomic composition after acid treatment (by ICP-AES) | surface atomic composition after acid treatment (by XPS) | length of Pd-rich NWs, by TEM (nm) | diameter of Pd-rich NWs, by TEM (nm) | lattice parameter, by XRD (Å) |
|---|---|---|---|---|---|---|---|
| Pd/C | | | | | | 4.2[a] | 3.891 |
| $Pd_1Fe_1$-NL | $Pd_{0.98}Fe_1$ | $Pd_2Fe_1$ | $Pd_{16.8}Fe_1$ | $Pd_{17.3}Fe_1$ | 100 | 1.8 | 3.888 |
| $Pd_2Fe_1$-NL | $Pd_{1.97}Fe_1$ | | $Pd_{11.4}Fe_1$ | | 60 | 2.0 | 3.880 |
| $Pd_5Fe_1$-NL | $Pd_{4.92}Fe_1$ | | | | 30 | 2.3 | 3.885 |

[a] Determined by Pd(220) peak in the XRD patterns using the Debye−Scherrer formula.

catalyst at room temperature. 1.0 mg of the deposited catalyst was dispersed in 1.0 mL ethanol and ultrasonically treated for 5 min, to make a uniform ink. The working electrode was prepared by dropping 20 $\mu$L of the catalyst ink on the GCE, which was subsequently covered by 10 $\mu$L of 0.05 wt % Nafion. For the Pd/C, 20 $\mu$L of the catalyst ink with 1.0 mg Pd/C/mL ethanol was used.

The CV tests were performed from −0.87−0.50 V (vs. Hg/HgO) for 20 cycles on the catalysts in high-purity $N_2$ (99.999%) saturated 1.0 M NaOH with a sweep rate of 50 mV/s. The electrochemical surface area (ECSA) was calculated based on the PdO reduction peak instead of the hydrogen desorption peak, according to refs 13f and 13g. For the ORR activity test, a linear scan from −0.80−0.20 V (vs Hg/HgO) was conducted on the catalyst in 0.1 M NaOH under high-purity $O_2$ (99.999%) bubbling. The sweep rate was 10 mV/s. All the electrochemical tests were conducted at room temperature and ambient pressure. The kinetic current ($i_k$) was calculated using eq 1, which is derived from the Levich−Koutecky (L-K) equation:[16]

$$i_k = \frac{i \times i_d}{i_d - i} \quad (1)$$

where $i$ is the observed current, and $i_d$ is the diffusion limiting current, which was collected at the region lower than −0.3 V (vs Hg/HgO). The mass activity was calculated by normalizing the kinetic current with the total PGM loading on the GCE.

## RESULTS AND DISCUSSION

The bulk chemical compositions of $Pd_xFe_y$-NL/C catalysts were determined by ICP-AES. As shown in Table 1, the Pd:Fe atomic ratio in the $Pd_xFe_y$-NL catalysts is 0.98:1 for $Pd_1Fe_1$-NL, 1.97:1 for $Pd_2Fe_1$-NL, and 4.92:1 for $Pd_5Fe_1$-NL. Note that the initially injected $Fe(CO)_5$ was only partially incorporated into the $Pd_xFe_y$-NL catalysts, i.e., only 0.51 mmol Fe was incorporated in $Pd_1Fe_1$-NL at an injection of 1.0 mmol $Fe(CO)_5$. This is due to the evaporation of a portion of the $Fe(CO)_5$ at the aging temperature of 160 °C, which is higher than its boiling point of 104 °C.[17]

The XRD patterns of the $Pd_xFe_y$-NL/C and Pd/C catalysts are shown in Figure 1a. Both Pd/C and $Pd_xFe_y$-NL/C catalysts displayed a typical face-centered cubic (fcc) XRD pattern. However, the diffraction peaks for each of the $Pd_xFe_y$-NL/C catalysts were slightly shifted to a higher $2\theta$ (Figure 1b), indicating that some Fe atoms may substitute in the Pd lattice, forming an alloy. No obvious diffraction peaks for Fe, $Fe_2O_3$, or other Fe oxides were observed in the XRD data of the $Pd_xFe_y$-NL/C catalysts, which suggests that most of the Fe (primarily associated with the Fe-rich sheets, described in detail in the following sections) was either amorphous in nature or fine-scaled

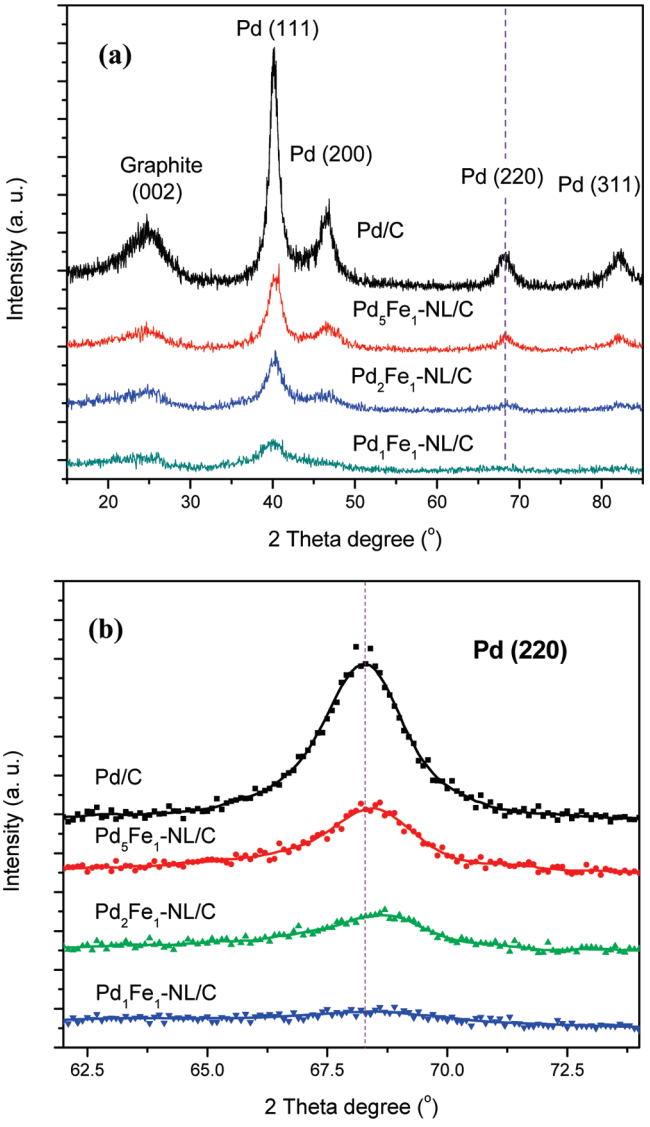


**Figure 1.** (a) XRD patterns comparing of Pd/C and $Pd_xFe_y$-NL/C samples with different PdFe compositions produced by the solution-phase reduction method. (b) Detailed Pt(220) diffraction peaks.

nanocrystalline. The average Pd particle size obtained from the Pd(220) peak using the Debye−Scherrer formula is 4.2 nm, while the broader Pd diffraction peaks associated with the


dx.doi.org/10.1021/cm1034134 |Chem. Mater. 2011, 23, 1570–1577

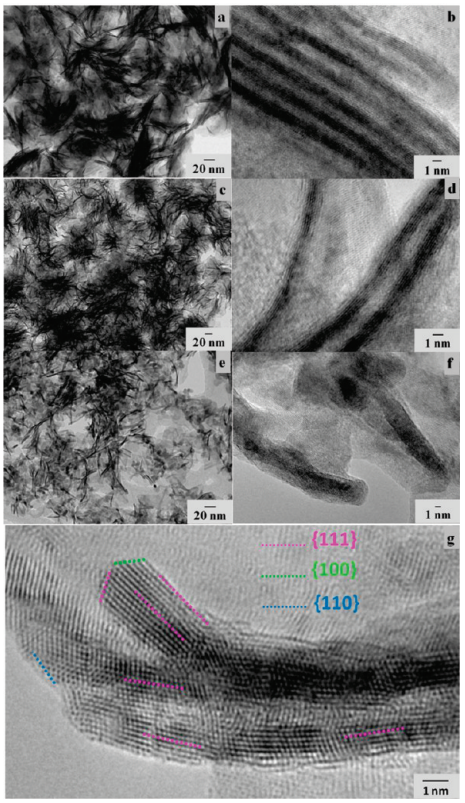


**Figure 2.** TEM images of the $Pd_xFe_y$-NLs: (a,b) $Pd_1Fe_1$-NL, (c,d) $Pd_2Fe_1$-NL, (e,f) $Pd_5Fe_1$-NL, and (g) HRTEM image of $Pd_1Fe_1$-NL.

$Pd_xFe_y$-NLs/C indicate the Pd-NWs in $Pd_xFe_y$-NLs have smaller diameters (compared to Pd/C).

Our previous research demonstrated that one-dimensional (1-D) PdFe bimetallic nanorods (NRs) with tunable lengths could be produced in an OAm and 1-Octadecne (ODE) system.[3g] (Note: We define nanowires and nanorods based on their aspect ratio, where the NW aspect ratio is ≥25 and the NR aspect ratio is <25.) By using pure OAm as stabilizer and solvent, 50-nm-length PdFe-NRs with a diameter of 2−3 nm were produced. With an increased ratio of OAm to ODE of 1:1, PdFe-NRs having a diameter of 3 nm and shorter lengths of 10 nm were synthesized. Using an OAm and ODE ratio of 1:3, uniformly dispersed PdFe nanoparticles with an average particle size of 2−4 nm were obtained. We observed that the PdFe-NRs were intimately mixed with a sheetlike flaky material; however, additional physical characterization was required to identify the nature of this flaky material. In the present study, we show that long Pd-rich NWs assembled on Fe-rich sheets form a novel nanoleave structure that can be achieved through a similar synthesis procedure as used to produce the PdFe-NRs.

Figure 2 shows TEM images of $Pd_xFe_y$-NLs with different Pd:Fe atomic ratios of 1:1, 2:1, and 5:1. It is clearly observed that the amount of the sheetlike material in the NLs was reduced when smaller amounts of Fe were injected into the synthesis system, suggesting that the sheets are Fe-based phases and the Fe concentration (in the synthesis system) controls the morphology of the as-prepared nanowires embedded in the sheets. As shown in Figures 2 a and 2b, a higher Fe concentration results in long, thin, and straight Pd-NWs with a size of ca. 100 nm ×1.8 nm (length × diameter). As the Fe concentration is decreased by half, the size of Pd-NWs is ca. 60 nm × 2.0 nm, as shown in

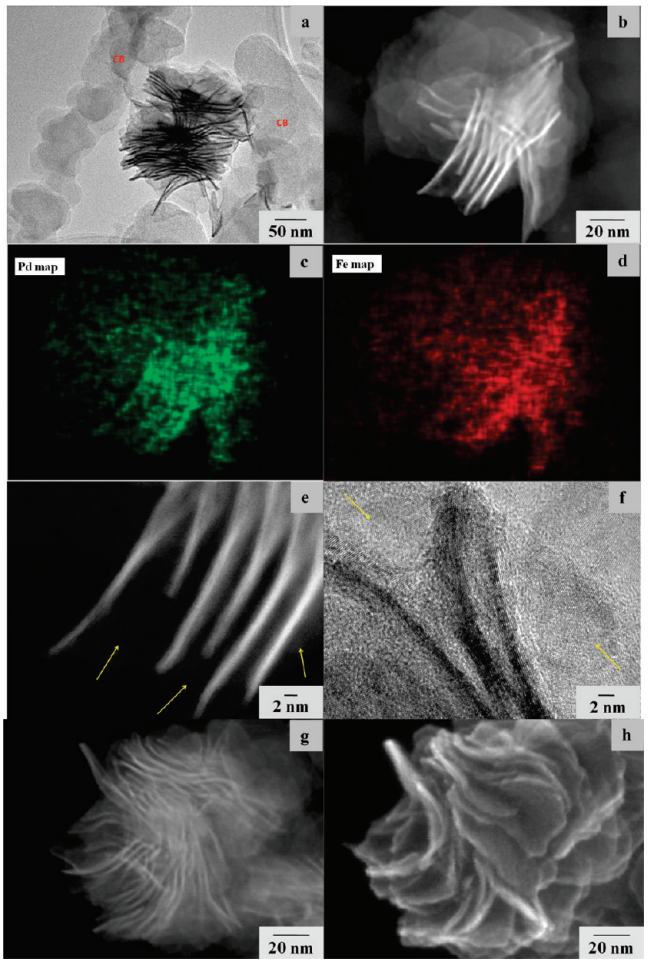


**Figure 3.** Morphology of $Pd_1Fe_1$-NLs/C: (a) TEM image, (b) HAADF-STEM image, (c and d) corresponding elemental maps for Pd and Fe (HR-EDS); (e) HAADF-STEM image and (f) TEM image showing NWs encapsulated by Fe-rich sheets (designated by yellow arrows), (g) HAADF-STEM image, and (h) corresponding SEM image showing the encapsulation of Pd-NWs in $Pd_1Fe_1$-NL and its topography.

Figure 2 c and 2d. A further decrease of the Fe content to 20% of the current load leads to shorter and slightly wider nanorods with a size of ca. 30 nm × 2.3 nm, as shown in Figure 2e and 2f. Therefore, decreasing the Fe content results in the formation of 1-D Pd nanostructures with shorter lengths and larger diameters. A typical HR-TEM image of the Pd-NWs in the $Pd_1Fe_1$-NL sample is shown in Figure 2g, which clearly shows that the side surfaces of the Pd-NWs are predominantly Pd(111) planes, while Pd(110) and Pd(100) planes are at the ends and tips of the NWs. Note that the morphology of PdFe-NLs is distinctively different from the Pd nanorods with larger diameter (5−10 nm) prepared using PVP as a stabilizer, where the side planes were predominantly Pd(110).[18] This could be attributed to their different 1-D nanostructure growth mechanisms (as discussed below), resulting from different synthesis conditions, i.e., different surfactants, presence/absence of Fe, etc.

To avoid NL agglomeration, the $Pd_xFe_y$-NLs were deposited on carbon black XC-72R before acid treatments. The morphology, compositional architecture, and crystalline structure of $Pd_xFe_y$-NLs/C were compared to the as-prepared $Pd_xFe_y$-NLs. As shown in Figure 3a, the $Pd_1Fe_1$-NLs were well-attached to the carbon black (CB) support. The HR-EDS elemental map shown


dx.doi.org/10.1021/cm1034134 |*Chem. Mater.* 2011, 23, 1570–1577

in Figures 3b−d differentiate the Pd-rich-NW veins (Pd map shown in green) and the Fe-rich-sheets (Fe map shown in red) of the nanoleaves. Note that there is an overlap between the Pd and Fe, indicating that a small amount of Pd is in the Fe-rich sheets and that the Fe-rich sheets encapsulate the Pd-NWs. The encapsulation of the NWs by the Fe-rich sheets is also evident from HAADF-STEM and TEM images in Figures 3e and 3f, where the thin Fe-rich layers surround the Pd-NWs. In addition, a direct comparison between simultaneously acquired HAADF-STEM (Figure 3g) and SEM (Figure 3h) images clearly show this encapsulation effect, where the HAADF-STEM image predominantly emphasizes the high atomic number NWs within the NL structure and the SEM image shows the topography (sheetlike encapsulation) of the NL.

The XPS spectra for the $Pd_1Fe_1$-NL/C sample are shown in Figure S1 in the Supporting Information. The large-range XPS survey clearly shows that Pd, Fe, and C, as well as trace amounts of S and N, originate from the carbon black and adsorbed OAm, respectively. Because the as-prepared NLs were exposed to air, O was also detected. The atomic ratio of Pd and Fe, which was calculated based on narrow scans at 329−347 eV and 700−740 eV, is close to 2:1. It is interesting to observe that the surface atomic ratio of Pd: Fe determined from XPS is twice that of the bulk composition obtained from ICP-AES (Pd:Fe = 0.98:1). Because XPS measures the topmost several nanometers of material, the difference of atomic ratios from XPS and ICP is consistent with a higher concentration of Pd on the Fe substrates in the NLs. Combining the evidence for encapsulation of Pd-NWs by Fe-rich sheets from the HAADF-STEM and TEM analysis, with the Pd−Fe composition from the XPS and ICP-AES results, we can reveal that the $Pd_xFe_y$-NLs has a unique structure with Fe-rich sheets as substrate and Pd-rich NWs assembled on the substrate.

Based on the characterization results presented, we propose a mechanism for the formation of the PdFe nanoleaves. $Pd(acac)_2$ is dissolved in OAm with a quick injection of $Fe(CO)_5$ at 105 °C, which facilitates fast Pd nucleation and produces a high density of Pd nuclei. This process is evidenced by an immediate color change from bright yellow to black. The optimized temperature promotes a balance between the formation of new Pd atoms and the addition of Pd atoms on existing Pd nuclei. The OAm in the system works as a solvent, surfactant, and reducing agent.[4j,k] To facilitate the generation of Pd(111) surface planes in previously published work,[4k] the OAm will selectively bond on Pd(111) facets, leading to a higher surfactant density on these surfaces. Pd atoms are therefore more easily attached or added on the Pd(100) and Pd(110) facets at the NW ends, which have less surfactants, resulting in the elongation of the nanowire parallel to the Pd(111) surface facets. $Fe(CO)_5$ injected into the system also facilitates the formation of uniform Pd-NWs. Without $Fe(CO)_5$, the main products in pure OAm system are Pd nanoparticles.[4k] In the present study, it is also observed that short rods and nanoparticles coexist in the $Pd_5Fe_1$-NL sample. Unlike Pt, which can form a PtFe alloy NW through spin−orbit coupling and hybridization between Fe 3d and Pt 5d,[4j,17] Pd seems more likely to form NWs with very small amounts of Fe dissolved Fe, which is evidenced by slight shifts observed for the Pd(220) peak by XRD (less formation of a PdFe alloy structure) in Figure 1 and from the HR-EDS elemental maps shown in Figure 4. Because OAm is not a strong ligand for Fe,[4i] Fe atoms prefer to grow as Fe-rich sheets, which is supported by the fact that less Fe-rich sheets are observed with decreasing Fe

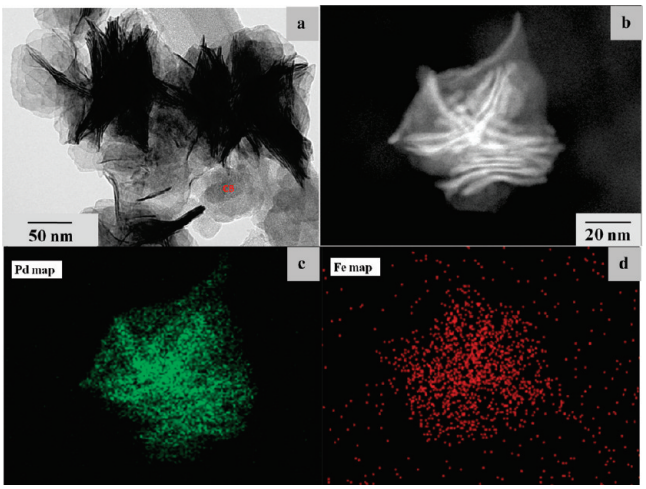


**Figure 4.** Morphology of $Pd_1$-NL/C ($Pd_1Fe_1$−NL/C after acid treatment): (a) TEM image, (b) HAADF-STEM image, (c) corresponding elemental map for Pd (HR-EDS), and (d) corresponding elemental map for Fe (HR-EDS).

concentration, as shown in Figures 2a, 2c, and 2e. For the Pd fcc structure, the surface energy of low-index crystallographic facets in vacuum follows a sequence of $\gamma(111) < \gamma(100) < \gamma(110)$, where Pd atoms are expected to nucleate and grow into cuboctohedral or quasi-spherical seeds with a mixture of (111) and (100) facets, to minimize the total surface energy.[8b,18] Under the synthesis conditions described herein, the Pd-NWs in PdFe-NLs were enveloped in Fe-rich sheets, which may effectively prohibit the deformation or breakage of the Pd-NWs to convert into Pd nanoparticles with a surface energy balance between (111) and (100) facets. This further suggests that thin and long Pd nanowires are able to maintain a predominance of surface Pd(111) planes, which cannot be achieved by Pd nanoparticles with a cuboctohedron shape. When the Fe amount decreased to one-half of that of Pd, not enough Fe sheets were formed to protect the long and straight Pd-NWs from deformation, leading to the formation of curved nanowires, as shown in Figure 2c. Further reduction in the Fe content would likely lead to reduced Fe-rich sheet formation, and result in the enhanced likelihood of breakage and rearrangement of Pd-NWs, which is evidenced by the formation of shorter and thicker Pd nanorods, as shown in Figure 2e.

To further clarify the proposed nanoleaves growth mechanism, we investigated the effects of injecting $Fe(CO)_5$ on the formation of the $Pd_1Fe_1$-NLs. For these experiments, sample $Pd_1Fe_1$-NL-B was prepared by mixing $Pd(acac)_2$ and $Fe(CO)_5$ at 60 °C. Sample PdFe-NL-C was produced by the injection of $Fe(CO)_5$ after reducing $Pd(acac)_2$ at 105 °C for 20 min. The TEM images of $Pd_1Fe_1$-NL-B and $Pd_1Fe_1$-NL-C are shown in Figure S2 in the Supporting Information. Although Pd-NWs with small diameters of 2−3 nm are produced for each synthesis condition, the homogeneity of these two samples are not well controlled, compared to $Pd_1Fe_1$-NL, as shown in Figure S2 in the Supporting Information. Reducing the injection temperature of $Fe(CO)_5$ restricted the reduction rate of $Pd(acac)_2$, thus leading to a slow and continuous nucleation process, which resulted in a broader length distribution of Pd-NWs (see Figures S2a and S2b in the Supporting Information). On the other hand, immediately increasing the temperature after the quick injection of $Fe(CO)_5$ without further aging accelerates the decomposition of $Fe(CO)_5$. Therefore, serious PdFe-NRs entanglement/aggregation are

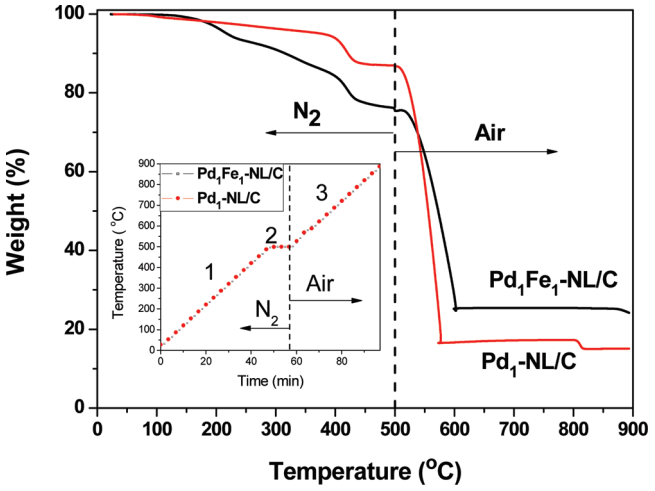


**Figure 5.** TGA curves and temperature ramp plots (insert) of $Pd_1Fe_1$-NL/C and $Pd_1$-NL/C ($Pd_1Fe_1$-NL/C after acid treatment).

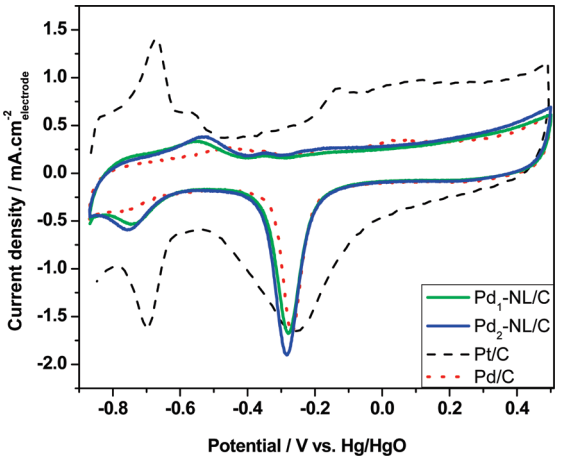


**Figure 6.** Cyclic voltammograms of commercial Pt/C, Pd/C (self-prepared by EG method), $Pd_1$-NL/C, and $Pd_2$-NL/C in 1.0 M NaOH, $N_2$-saturated (conditions: 50 mV/s, room temperature).

observed in the $Pd_1Fe_1$-NL-C sample (see Figures S2c and 2d in the Supporting Information).

Pd-rich NLs can be achieved by conducting an organic acid treatment to remove much of the Fe in the PdFe-NLs. After the acid treatment, the structure of the $Pd_1$-NL/C ($Pd_1Fe_1$-NL/C after acetic acid treatment) was characterized using SEM, HAAD-S/TEM, and HR-EDS elemental mapping. The TEM image in Figure 4a clearly shows that, after acid leaching, the NW structure is maintained in the NL structure without any observable morphology changes. HR-EDS elemental mappings were obtained to study the effects of acid treatment on the composition of the NL particles and are shown in Figures 4b−d. The removal of Fe is clearly shown, with most of the Fe confined to the center of the NL structure, while little change was observed for the Pd-NWs. Quantitative EDS analysis showed the overall $Pd_1$-NL has an atomic ratio of Pd:Fe = 16:1, which is in good agreement with the results of ICP-AES analysis (Pd:Fe = 16.8: 1). Since the ratio of Pd:Fe in the initial $Pd_1Fe_1$-NL is very close to 1:1, this indicates that a significant amount of the Fe phase has been removed and that nearly pure Pd-NWs remain in the NLs.

XPS characterization results for the acid-leached $Pd_1$−NL sample are shown in Figure S3 in the Supporting Information and confirm the significant removal of Fe from the $Pd_1Fe_1$-NL/C. The atomic ratio of Pd:Fe measured by XPS is 17.3:1, which is consistent with the ratio determined by both EDS and ICP-AES. The XPS analysis also shows a sharp decrease in N as a result of the acid treatment, from 1.6% to 0.4%, which could be attributed to the removal of surfactant OAm through the acid-leaching procedure. However, because of the adsorption of $N_2$ from the air, the N concentration determined by XPS cannot be used to determine the actual amount of residual surfactants.

The amount of surfactants removed by aid treatment was determined by comparing the thermogravimetric analysis (TGA) curves for $Pd_1Fe_1$-NL/C and $Pd_1$-NL/C, the results of which are shown in Figure 5. The first two steps were carried out from RT to 500 °C in inert $N_2$ gas, and the third step was from 500−900 °C in oxidative air (as shown in the inset in Figure 5). During the first two steps, the weight losses can be mainly attributed to the thermal decomposition of organic surfactants, taking into consideration of the good stabilities of Pd, Fe metal, and carbon black in $N_2$ in the conducted temperature range. Before the acetic acid treatment, the weight loss of $Pd_1Fe_1$-NL/C initiated at ∼125 °C and underwent a total loss of 24 wt % at ∼500 °C. However, after the acetic acid treatment, the weight loss of $Pd_1$-NL/C was only 13 wt %. The weight loss observed at ∼100 °C (Figure 5) for the $Pd_1$-NL/C was assigned to the evaporation of water adsorbed into the sample. However, the weight loss (at ∼100 °C) was not observed on the $Pd_1Fe_1$-NL/C, which was probably a result of the hydrophobic nature of OAm that covered the untreated $Pd_1Fe_1$-NL. The removal of OAm in organic acid is in agreement with prior work from other groups.[4k,9] The removal of OAm may be caused by the reaction between −COOH in acetic acid and $NH_2$− in OAm at an elevated temperature, i.e., at 70 °C in our study. The huge weight losses from observed from 500 °C to 600 °C were due to the rapid oxidation of the carbon black support in air. Because of the formation of metal oxides at higher temperature, a gradual weight increase and a small step afterward exists on $Pd_1$-NL/C in step 3, which are attributed to the oxidation of Pd and the decomposition of PdO to $Pd^0$, respectively.[19] Because of the encapsulation of Pd-NWs by Fe-rich sheets, this thermal decomposition peak associated with PdO is absent on $Pd_1Fe_1$-NL/C. Since the carbon black will be oxidized to $CO_2$ during TGA, the residual weight can be used to estimate the PdFe metal loading.[20] After the acid treatment, the metal loading of the $Pd_1$-NL/C and $Pd_2$-NL/C samples determined by TGA were reduced to 16.5 wt % and 18.9 wt %, respectively.

The electrocatalytic performance was investigated for the $Pd_1$-NL/C and $Pd_2$-NL/C ($Pd_1Fe_1$-NL/C and $Pd_2Fe_1$-NL/C after the acid treatment, respectively), and the results were compared with those evaluated for the Pd/C and commercial Pt/C catalysts. Figure 6 shows the cyclic voltammograms of the four catalysts recorded in $N_2$-saturated 1.0 M NaOH at a sweep rate of 50 mV/s. Because hydrogen can penetrate into the Pd lattices, the ECSAs of the Pd-based catalysts were calculated based on the charge of the reduction region of PdO/Pd at around −0.28 V (vs Hg/HgO) with the double-layer correction, assuming 0.405 mC/cm$^2$ for the reduction of a monolayer PdO on the catalyst surface.[13h,21] The specific ECSAs were 50.9, 51.4, and 35.5 $m^2/g_{Pd}$ for $Pd_1$-NL, $Pd_2$-NL, and Pd/C, respectively. The ECSA of Pt/C is 56.9 $m^2/g_{Pt}$, based on the calculation for the PtO reduction peak. The $Pd_x$-NLs have larger specific ECSAs, which are attributed to their ultrathin diameters (∼2 nm) of Pd-rich NWs in the Pd-NLs.


dx.doi.org/10.1021/cm1034134 |*Chem. Mater.* 2011, 23, 1570–1577

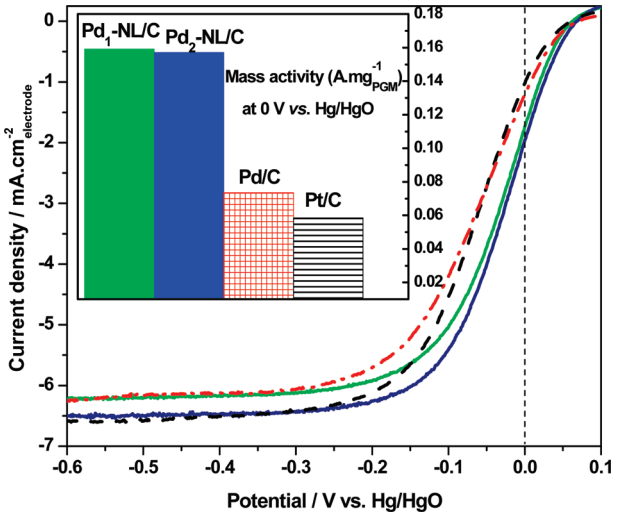


**Figure 7.** ORR polarization curves of commercial Pt/C, Pd/C (self-prepared by EG method), $Pd_1$-NL/C, and $Pd_2$-NL/C in 0.1 M NaOH, $O_2$ bubbling (conditions: 10 mV/s, 2500 rpm, room temperature).

The ORR polarization curves for the four catalysts are shown in Figure 7. While the Pd/C has a slightly higher ORR activity than the commercial Pt/C, the Pd-NLs show a remarkable improvement in ORR activity with the half-wave potential shifting positively by ~38 mV, compared to Pt/C. At 0 V vs Hg/HgO, the mass activity of $Pd_1$-NL and $Pd_2$-NL are 0.159 A/$mg_{Pd}$ and 0.157 A/$mg_{Pd}$, respectively, which are ~2× higher than that of Pd/C (0.0735 A/$mg_{Pd}$) and ~2.7× higher than that of Pt/C (0.0585 A/$mg_{Pt}$). Although the TGA curves indicate there still are some surfactants covering Pd-NLs even after the acid treatment, the specific activities of $Pd_1$-NLs and $Pd_2$-NLs at 0 V vs Hg/HgO were 312 and 305 $\mu$A/$cm_{Pd}^2$, respectively, which are higher than that of Pd/C (207 $\mu$A/$cm_{Pd}^2$) and Pt/C (103 $\mu$A/$cm_{Pt}^2$). Since the Pd/C was prepared by the EG method, its Pd surface is considerably clean (very little surfactant effects), the results indicate that small amount of surfactants (OAm) in the Pd-NLs catalysts will not affect the intrinsic ORR activities in alkaline electrolyte.

It has been determined that the electronic structure (d-band center, relative to the Fermi level) governs the strength of bonding of OH and O to a metal, and that, in turn, controls the ORR kinetics.[3c−e] Compared to transitional metals, Pt-group metals have advantageous electronic structures and generally possess higher ORR activity. Specifically, Pt and Pd exhibit higher ORR activity than other PGMs.[3,13e] In acid electrolytes, Pt has demonstrated an order-of-magnitude-higher intrinsic ORR activity than Pd at low overpotential (i.e., 0.9 V vs RHE), where the half-wave potential of the ORR curve for Pt/C is >50 mV higher than that for Pd/C.[11b,d] In alkaline electrolytes, however, Pd is reported to have an ORR activity very close to Pt. Lima et al[13e] investigated a series of metal single crystals and carbon-supported metal nanoparticle catalysts, including Pt, Pd, Rh, Ir, Ru, Au, and Ag. They found that, at 0.85 V (vs RHE, = −0.08 V vs Hg/HgO), Pt(111) and Pd(111) have ORR current densities of 1.8 mA/$cm^2$ and 1.2 mA/$cm^2$, respectively, which are higher than other PGM competitors, while the current density of Pt/C and Pd/C is 11.5 mA/$cm^2$ and 6.5 mA/$cm^2$, respectively, which can be converted to 0.58 A/$mg_{Pt}$ and 0.33 A/$mg_{Pd}$. Jiang et al.[13g,h] recently reported the apparent ORR activation energy in 0.1 M KOH for Pt/C and Pd/C are 48 and 40 kJ/mol, respectively, at an overpotential of 0.3 V, which indicates that the ORR kinetics for Pd are similar to Pt. For 0-D nanoparticle catalysts, there typically exists an optimum particle size with the highest mass activity,[22] which is a tradeoff between surface area, crystalline facets (with different intrinsic activity), and surface chemical state of Pt and Pd (surface oxidation of Pt and Pd could lead to catalytically inert PtO and PdO).[13g,h] As the Pd particle gets smaller than the optimum size, although its surface area increases, the ratio of Pd(111) to Pd(100) decreases and the surface is more prone to oxidation; therefore, its mass activity drops. The optimum Pd particle size has been found to be ~5.0 nm for the ORR in an alkaline electrolyte.[13g] In the present study, the Pd/C particle size of 4.2 nm (which is close to the reported optimum size) shows slightly higher ORR activity than Pt/C at 0 V Hg/HgO (0.93 V vs RHE), When the overpotential increases, the Pt/C exhibits a higher current density and reaches a higher limiting current density than Pd/C. The ORR activity baseline for Pt/C and Pd/C presented here is consistent with the previous study.

Compared to Pt/C and Pd/C catalysts, the much-improved ORR activity for Pd-NLs can be attributed to their unique high surface area and nanoleave structure. Previous studies have shown that 1-D catalysts, such as Pt-NWs and Pt-nanotubes (NTs), have enhanced ORR activity, because of the presence of a lower density of surface defects and unique surface electronic properties.[5b,6] However, their large dimensions, e.g., 200 nm in diameter for Pt-NWs[5b] and 4−7 nm wall thickness and 40−50 nm outer diameter for Pt-NTs,[6] resulted in a small electrochemical surface area, thus, limiting their mass activity enhancement. In comparison, the ultrathin Pd-NWs with a large aspect ratio reported here were uniformly covered by advantageous Pd(111) facets and maintained a large electrochemical surface area (i.e., >50 $m^2$/g in this study). In addition, the ultrathin Pd-NWs were textured in the NLs, which may also enhance the surface oxidation resistance. All these factors contribute to a high ORR mass activity for the Pd-NLs. The electrochemical performance of these novel Pd-NLs in real single anion exchange membrane fuel cell configuration is currently under study.

## CONCLUSIONS

In summary, a simple wet chemistry-based solution phase synthesis method has been developed to produce novel PdFe nanoleaves. A combination of characterization techniques has shown that this unique structure is composed of Pd-NWs "veins" assembled within Fe-rich "blades". The side surfaces of the enveloped Pd-NWs are predominantly Pd(111) facets, which are supported and protected by the Fe sheets and can not be easily changed. After an acetic acid treatment, the 1-D Pd-NWs with a diameter of ~2 nm and a large surface are of >50 $m^2$/g, can be exposed on the surfaces of NLs. The Pd-rich NLs demonstrated high reactivity toward electrocatalytic reduction of oxygen in a 0.1 M NaOH electrolyte and exhibited a 3.0× increase in specific activity and a 2.7× increase in mass activity, compared to those of a commercial Pt/C catalyst (at 0 V vs. Hg/HgO). The electrocatalytic activity enhancement can be attributed to the unique nanoleave structure, i.e., extensive Pd(111) facets, large surface area and more resistance to Pd oxide formation. The novel PdFe-NLs are a promising new class of cathode catalysts for anion exchange membrane fuel cells.

## ASSOCIATED CONTENT

**Supporting Information.** XPS spectra of $Pd_1Fe_1$-NL/C and $Pd_1$-NL/C, and TEM images of $Pd_1Fe_1$-NL-B and $Pd_1Fe_1$-NL-C.


dx.doi.org/10.1021/cm1034134 |*Chem. Mater.* 2011, 23, 1570–1577

This material is available free of charge via the Internet at http://pubs.acs.org.

## AUTHOR INFORMATION

**Corresponding Author**

*Tel.: 1-906-487-2298. Fax: 1-906-487-3213. E-mail: wzli@mtu.edu.

## ACKNOWLEDGMENT

We acknowledge the U.S. National Science Foundation (CBET-1032547) for funding. Acknowledgment is also made to the Donors of the American Chemical Society Petroleum Research Fund for partial support of this research. A portion of this research was supported by ORNL's Center for Nanophase Materials Sciences (CNMS) and SHaRE User Facilities, both of which are sponsored by the Office of Basic Energy Sciences, U.S. Department of Energy.

## REFERENCES

(1) (a) Vielstich, W.; Lamm, A.; Gasteiger, H. A. *Handbook of Fuel Cells: Fundamentals, Technology, Applications*; Wiley: New York, 2003. (b) Dresselhaus, M. S.; Thomas, I. L. *Nature* **2001**, *414* (6861), 332–337.

(2) (a) Yeager, E. *Electrochim. Acta* **1984**, *29* (11), 1527–1537.(b) Adzic, R. R. *Recent Advances in the Kinetics of Oxygen Reduction Reaction*; Wiley−VCH: New York, 1998. (c) Norskov, J. K.; Rossmeisl, J.; Logadottir, A.; Lindqvist, L.; Kitchin, J. R.; Bligaard, T.; Jonsson, H. *J. Phys. Chem. B* **2004**, *108* (46), 17886–17892. (d) Gasteiger, H. A.; Kocha, S. S.; Sompalli, B.; Wagner, F. T. *Appl. Catal., B* **2005**, *56* (1−2), 9–35. (e) Stamenkovic, V. R.; Fowler, B.; Mun, B. S.; Wang, G. F.; Ross, P. N.; Lucas, C. A.; Markovic, N. M. *Science* **2007**, *315* (5811), 493–497.

(3) (a) Ahmadi, T. S.; Wang, Z. L.; Green, T. C.; Henglein, A.; Elsayed, M. A. *Science* **1996**, *272*, 1924–1926. (b) Bell, A. T. *Science* **2003**, *299*, 1688–1691. (c) Tian, N.; Zhou, Z. Y.; Sun, S. G.; Ding, Y.; Wang, Z. L. *Science* **2007**, *316* (5825), 732–735. (d) Alayoglu, S.; Nilekar, A. U.; Mavrikakis, M.; Eichhorn, B. *Nat. Mater.* **2008**, *7* (4), 333–338. (e) Tian, N.; Zhou, Z. Y.; Sun, S.-G. *J. Phys. Chem. C* **2008**, *112*, 19801–19817. (f) Xie, X. W.; Li, Y.; Liu, Z. Q.; Haruta, M.; Shen, W. J. *Nature* **2009**, *458* (7239), 746–749. (g) Li, W. Z.; Haldar, P. *Electrochem. Commun.* **2009**, *11* (6), 1195–1198.

(4) (a) Astruc, D. *Transition-Metal Nanoparticles in Catalysis*; Wiley−VCH: New York, 2007. (b) Toshima, N.; Yonezawa, T. *New J. Chem.* **1998**, *22* (11), 1179–1201. (c) Zhao, M. Q.; Crooks, R. M. *Adv. Mater.* **1999**, *11* (3), 217–222. (d) Murray, C. B.; Kagan, C. R.; Bawendi, M. G. *Annu. Rev. Mater. Sci.* **2000**, *30*, 545–610. (e) Jana, N. R.; Gearheart, L.; Murphy, C. J. *Adv. Mater.* **2001**, *13* (18), 1389–1393. (f) Bonnemann, H.; Richards, R. M. *Eur. J. Inorg. Chem.* **2001**, *10*, 2455–2480. (g) Sun, Y. G.; Xia, Y. N. *Science* **2002**, *298* (5601), 2176–2179. (h) Roucoux, A.; Schulz, J.; Patin, H. *Chem. Rev.* **2002**, *102* (10), 3757–3778. (i) Chen, M.; Kim, J.; Liu, J. P.; Fan, H. Y.; Sun, S. H. *J. Am. Chem. Soc.* **2006**, *128* (22), 7132–7133. (j) Wang, C.; Hou, Y. L.; Kim, J. M.; Sun, S. H. *Angew. Chem., Int. Ed.* **2007**, *46* (33), 6333–6335. (k) Mazumder, V.; Sun, S. H. *J. Am. Chem. Soc.* **2009**, *131* (13), 4588–4589.

(5) (a) Sun, S. H.; Jaouen, F.; Dodelet, J. P. *Adv. Mater.* **2008**, *20* (20), 3900–3903. (b) Zhou, H.; Zhou, W.-P.; Adzic, R. R.; Wong, S. S. *J. Phys. Chem. C* **2009**, *113*, 5460–5466.

(6) Chen, Z. W.; Waje, M.; Li, W. Z.; Yan, Y. S. *Angew. Chem., Int. Ed.* **2007**, *46* (22), 4060–4063.

(7) (a) Wang, J. X.; Inada, H.; Wu, L. J.; Zhu, Y. M.; Choi, Y. M.; Liu, P.; Zhou, W. P.; Adzic, R. R. *J. Am. Chem. Soc.* **2009**, *131* (47), 17298–17302. (b) Mazumder, V.; Chi, M. F.; More, K. L.; Sun, S. H. *J. Am. Chem. Soc.* **2010**, *132* (23), 7848–7849.

(8) (a) Lim, B.; Jiang, M. J.; Camargo, P. H. C.; Cho, E. C.; Tao, J.; Lu, X. M.; Zhu, Y. M.; Xia, Y. A. *Science* **2009**, *324* (5932), 1302–1305. (b) Lim, B.; Jiang, M. J.; Tao, J.; Camargo, P. H. C.; Zhu, Y. M.; Xia, Y. N. *Adv. Funct. Mater.* **2009**, *19* (2), 189–200.

(9) Peng, Z. M.; Wu, J. B.; Yang, H. *Chem. Mater.* **2010**, *22* (3), 1098–1106.

(10) Element Pt & Element Pd. http://environmentalchemistry.com/yogi/periodic.

(11) (a) Savadogo, O.; Lee, K.; Oishi, K.; Mitsushima, S.; Kamiya, N.; Ota, K. I. *Electrochem. Commun.* **2004**, *6* (2), 105–109. (b) Zhang, J. L.; Mo, Y.; Vulkmirdvic, M. B.; Klie, R.; Sasaki, K.; Adzic, R. R. *J. Phys. Chem. B* **2004**, *108*, 10955–10964. (c) Fernandez, J. L.; Raghuveer, V.; Manthiram, A.; Bard, A. J. *J. Am. Chem. Soc.* **2005**, *127* (38), 13100–13101. (d) Shao, M. H.; Sasaki, K.; Adzic, R. R. *J. Am. Chem. Soc.* **2006**, *128* (11), 3526–3527.

(12) (a) O'Hayre, R.; Cha, S.-W.; Colella, W; Prinz, F. B. *Fuel Cell Fundamentals*; John Wiley & Sons, Inc.: New York, 2006. (b) Markovic, N. M.; Ross, P. N. *Surf. Sci. Rep.* **2002**, *45*, 117–229.

(13) (a) Meadowcroft, D. B. *Nature* **1970**, *226*, 2–4. (b) Spendelow, J. S.; Wieckowski, A. *Phys. Chem. Chem. Phys.* **2007**, *9* (21), 2654–2675. (c) Markovic, N. M.; Gasteiger, H. A.; Philip, N. *J. Phys. Chem. B* **1996**, *100* (16), 6715–6721. (d) Climent, V.; Markovic, N. M.; Ross, P. N. *J. Phys. Chem. B* **2000**, *104* (14), 3116–3120. (e) Lima, F. H. B.; Zhang, J.; Shao, M. H.; Vukmirovic, M. B.; Ticianelli, E. A.; Adzic, R. R. *J. Phys. Chem. B* **2007**, *111*, 404–410. (f) Li, B.; Prakash, J. *Electrochem. Commun.* **2009**, *11* (6), 1162–1165. (g) Jiang, L.; Hsu, A.; Chu, D.; Chen, R. *J. Electrochem. Soc.* **2009**, *156* (5), B643–B649. (h) Jiang, L.; Hsu, A.; Chu, D.; Chen, R. *J. Electrochem. Soc.* **2009**, *156* (3), B370–B376.

(14) (a) Varcoe, J. R.; Slade, R. C. T. *Fuel Cells* **2005**, *5* (2), 187–200. (b) Agel, E.; Bouet, J.; Fauvarque, J. F. *J. Power Sources* **2001**, *101* (2), 267–274. (c) Lu, S. F.; Pan, J.; Huang, A. B.; Zhuang, L.; Lu, J. T. *Proc. Natl. Acad. Sci. U.S.A.* **2008**, *105* (52), 20611–20614. (d) Gu, S.; Cai, R.; Luo, T.; Chen, Z.; Sun, M.; Liu, Y.; He, G.; Yan, Y. *Angew. Chem., Int. Ed.* **2009**, *48* (35), 6499–6502. (e) Gu, S.; Cai, R.; Luo, T.; Jensen, K.; Contreras, C.; Yan, Y. S. *ChemSusChem* **2010**, *3* (5), 555–558.

(15) (a) Li, W. Z.; Liang, C. H.; Qiu, J. S.; Zhou, W. J.; Han, H. M.; Wei, Z. B.; Sun, G. Q.; Xin, Q. *Carbon* **2002**, *40*, 791–794. (b) Li, W. Z.; Liang, C. H.; Zhou, W. J.; Qiu, J. S.; Zhou, Z. H.; Sun, G. Q.; Xin, Q. *J. Phys. Chem. B* **2003**, *107*, 6292–6299. (c) Zhou, Z. H.; Wang, S. L.; Zhou, W. J.; Wang, G. X.; Jiang, L. H.; Li, W. Z.; Song, S. Q.; Liu, J. G.; Sun, G. Q.; Xin, Q. *Chem. Commun.* **2003**, *1*, 394–395.

(16) Paulus, U. A.; Wokaun, A.; Scherer, G. G.; Schmidt, T. J.; Stamenkovic, V.; Radmilovic, V.; Markovic, N. M.; Ross, P. N. *J. Phys. Chem. B* **2002**, *106* (16), 4181–4191.

(17) Sun, S. H.; Fullerton, E. E.; Weller, D.; Murray, C. B. *IEEE Trans. Magn.* **2001**, *37* (4), 1239–1243.

(18) (a) Xiong, Y. J.; Xia, Y. N. *Adv. Mater.* **2007**, *19* (20), 3385–3391. (b) Xiong, Y. J.; Cai, H. G.; Wiley, B. J.; Wang, J. G.; Kim, M. J.; Xia, Y. N. *J. Am. Chem. Soc.* **2007**, *129* (12), 3665–3675.

(19) Groppi, G.; Cristiani, C.; Lietti, L.; Ramella, C.; Valentini, M.; Forzatti, P. *Catal. Today* **1999**, *50* (2), 399–412.

(20) Li, W. Z.; Chen, Z. W.; Xu, L. B.; Yan, Y. *J. Power Sources* **2010**, *195* (9), 2534–2540.

(21) Nguyen, S. T.; Law, H. M.; Nguyen, H. T.; Kristian, N.; Wang, S. Y.; Chan, S. H.; Wang, X. *Appl. Catal., B* **2009**, *91* (1−2), 507–515.

(22) (a) Peuckert, M.; Yoneda, T.; Betta, R. A. D.; Boudart, M. *J. Electrochem. Soc.* **1986**, *133* (5), 944–947. (b) Kinoshita, K. *J. Electrochem. Soc.* **1990**, *137* (3), 845–848.